Longitudinal impedance and coherent synchrotron radiation models for ThomX storage ring

A. Gamelin, E. Ergenlik, D. Le Guidec, H. Monard, C. Bruni

Version of Record: https://www.sciencedirect.com/science/article/pii/S0168900221001753
Manuscript_388b9f81ea2841105983989283dd8a61

Longitudinal impedance and coherent synchrotron radiation models for ThomX storage ring

A. Gamelin[a,b], E. Ergenlik[a], D. Le Guidec[a], H. Monard[a], C. Bruni[a]

[a] *LAL, Univ. Paris-Sud, CNRS/IN2P3, Université Paris-Saclay, Orsay, France*
[b] *Synchrotron SOLEIL, France*

Abstract

This article deals with the design of an impedance model (including geometric, resistive wall and coherent synchrotron radiation (CSR) wakefields) for ThomX, a 50 MeV electron storage ring designed to work in pulsed mode. The beam dynamics is very different from usual damped storage rings and is strongly dominated by collective effects. The geometric and resistive wall impedance model is obtained using simulation or analytical modelling of the individual elements and is checked using wire measurements on prototypes. The CSR is simulated in a rectangular vacuum chamber to take into account transient effects and resonances. From these models, two distinct regimes of beam dynamics stand out, driven respectively by the CSR and by the geometric impedance.

Keywords: Beam coupling impedance, Coherent synchrotron radiation, Wire measurement, Wakefield

1. Introduction

ThomX is a compact laser-electron storage rings (LESR) [1], a Compton backscattering X-ray source, which is being built at LAL, Orsay, France [2, 3]. ThomX storage ring design parameters are shown in Table 1. In this machine, electrons are accelerated and injected into a storage ring where they interact

Email addresses: gamelin@synchrotron-soleil.fr (A. Gamelin), corresponding author : bruni@lal.in2p3.fr (C. Bruni)
now merged into IJCLab

with a laser to produce 1×10^{13} photons per second in the hard X-ray range (50 to 90 KeV). As usual in LESR, such as TTX-II [4], NESTOR [5] or ThomX, the beam can suffer from strong degradation by single, multiple Touschek scattering and Compton interaction. To counter this effect, the machine works in pulsed mode: a new bunch is injected every 20 ms while the older one is extracted [6]. The global aim of the machine is to maximise the X-ray flux produced by taking care of the spectral and angular flux [7]. The electron storage ring has been designed with this intent which makes the electron beam dynamics very different from the beam dynamics in usual storage rings dedicated to synchrotron radiation production [8, 6, 9, 10]. The difference results from damping times long compared to the storage time. As the electron dynamics is not damped, it is crucial to manage the collective effects (defined as the interaction of the particles with each other as well as with its environment) as, once the beam is perturbed it will not recover within the storage time. In addition, the beam is injected without longitudinal matching and the lattice has a strong nonlinear dependence on energy of the momentum compaction. Due to the previous considerations, the bunch undergoes a transient regime of filamentation at injection until it has fully filled the RF bucket [6]. Besides, the injected electron bunch has a low energy, 50 MeV, a relatively high charge, 1 nC, and a short duration, a few ps, which implies very strong collective effects. In particular, the coherent synchrotron radiation (CSR) is expected to play a strong role during the transient regime as the injected bunch length is short. After the transient regime, the bunch length is much longer and the CSR impact is expected to be much more reduced compared to the geometric and resistive walls (RW) wakefields.

During the design phase of an accelerator project, the different beam coupling impedance sources should be estimated and summarised in an impedance budget. The impedance bugdet can then be used to ensure that the wakefields will not prevent achieving nominal performances, which for ThomX means avoiding any degradation on the X-rays flux or quality. Also, a good knowledge of the machine impedance allows for a better discrimination of possible instability sources. Unfortunately strong discrepancies have been noted between

Table 1: ThomX nominal storage ring design parameters. The range of values given for the emittance, the relative energy spread and the bunch duration correspond to typical beam properties at injection depending on the linac setup.

Parameter	**Value**	**Units**
Beam energy E_0	50	MeV
Emittance (rms, normalised) $\epsilon_{x,y}$	7 - 9	mm.mrad
Rel. energy spread at inj. (rms) σ_δ	0.2 - 0.6	%
Bunch duration at inj. (rms) σ_s	6 - 16	ps
Bunch charge Q	1	nC
Circumference L_0	18	m
Number of bunch	1	
Current I	16.7	mA
Trans./long. damping time $\tau_{x,y}/\tau_s$	1/0.5	s
Momentum compaction factor α_1	0.0124	
Tune x/y, Q_x/Q_y	3.17/1.74	
Storage time before ext./inj. T_{store}	20	ms

measured data and prediction based on computed impedance budgets [11]. A way to check the impedance estimations, obtained by numeric simulation or by analytic development, is to use bench measurements [12, 13]. As a basis for future complete analysis of the beam dynamics in the presence of collective effects, we present in this paper the simulated and measured impedance models for the geometric, resistive walls and CSR wakefields for ThomX storage ring. We show that the CSR is dominant with respect to impedance during the transient regime when the bunch length is short. After the transient regime, the bunch length is much longer and the CSR impact is reduced compared to the geometric and RW wakefields.

The geometric and RW model has been obtained using either numerical simulations or an analytical model for each of the different components. It is presented in section 2. The simulations have then been cross-checked against bench measurements using the coaxial wire method, the measurement results are shown in section 3 and the detailed error estimate is presented in appendix. Finally, the CSR has been simulated, taking into account rectangular chamber and drifts, using the CSRZ code [14] and the results are presented in section 4.

2. ThomX RW and geometric impedance model

When it was possible, the storage ring elements have been simulated using CST [15] up to 50 GHz corresponding to a bunch length of $\sigma_z = 2\,\mathrm{mm}$, which is the bunch length at injection. For higher frequencies, the geometric impedance contribution is much smaller than the CSR one and thus can be neglected in the specific case of ThomX. CST wakefield solver can be used to compute the fields generated by a beam when said beam is going trough 3D structures. It takes into account both of the geometric and the resistive wall wakefields and has been benchmarked multiple times against theory and other codes [15, 16]. When numerical simulation was not possible, due to thin coating on kicker magnets, an analytic model was used.

The plots of the real part and of the imaginary part of the longitudinal impedance $Z_\parallel$ are shown in Fig. 1. The contribution of each element type is represented by the different coloured areas. The summary of the impedance budget is shown in Table 2. The loss factor $k_\parallel$ for each individual element is computed for a $\sigma = 2\,\mathrm{mm}$ bunch and the relative contribution of each type to the total loss factor $k_{\parallel,T} = 6.73\,\mathrm{V\,pC^{-1}}$ is shown. We will now go through the contribution of each element.

Table 2: Summary of all the elements composing ThomX storage ring and of their relative contribution to the impedance budget. Loss factor $k_\parallel$ computed for a Gaussian longitudinal distribution of $\sigma_z = 2\,\mathrm{mm}$.

Element	**Number**	$\boldsymbol{k_\parallel}$ (V/pC)	**% of** $\boldsymbol{k_{\parallel,T}}$
Bellows	18	1.54×10^{-2}	4.1 %
BPMs	12	3.59×10^{-2}	6.3 %
IP clearing electrodes	2	1.20×10^{-2}	0.4 %
IP chamber	1	1.23×10^{-1}	1.8 %
Pumping ports	15	4.13×10^{-2}	9.2 %
Kickers	2	4.1×10^{-1}	12.2 %
Septum	1	1.14	17.0 %
FBT	1	1.52×10^{-1}	2.3 %
RF Cavity + Tapers	1	3.14	46.7 %
Total		$k_{\parallel,T} = 6.73$	100 %

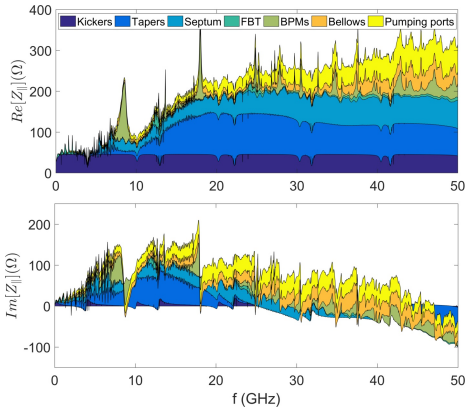

Figure 1: Real and imaginary part of the longitudinal impedance $Z_{\|}$ for ThomX storage ring (without the RF cavity contribution). Each component contribution to the total impedance is represented by a coloured area. The full sum corresponds to the upper limit of the yellow (pumping ports) area.

2.1. Bellows, BPMs and pumping ports

ThomX beam pipe has an octagonal cross section and most of the elements have the same shape to avoid impedance increase due to tapered sections. The bellows have integrated RF fingers with the same octagonal cross section in order to shield the beam from the irregular surface of the bellows, see Fig. 2. The 18 bellows of the storage ring amount to 4.1 % of the total loss factor $k_{\|,T}$.

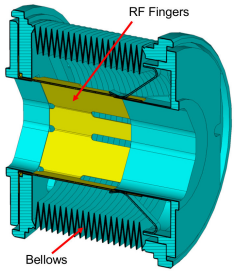

Figure 2: CST model of the bellows with RF fingers.

There are different types of beam position monitors (BPMs) in ThomX storage ring. Their design is based on SOLEIL BPMs [17, 18], which is a classic button BPM bloc with four electrodes. In ThomX, some BPMs have double

BPM blocs with six or hight electrodes. The additional buttons are used as ion clearing electrodes to avoid ion trapping by the electron beam [8, 19]. In a button BPM, the electromagnetic fields excited by the beam can be trapped in the structure. There are two main trapped modes, at 8.6 GHz and at 18.0 GHz, which correspond to the modes created between the BPM button and the BPM bloc housing the button. The fields can also propagate and resonate in the dielectric material composing the vacuum insulator and act back on the beam. These resonant modes, located around 14 GHz, have a lower amplitude compared to the main ones. The loss factor value in Table 2 for the BPMs corresponds to a double BPM bloc with six buttons.

2.2. Interaction point

In addition to BPM, there are also two stand-alone clearing electrodes located at the interaction point (IP) and at the point symmetric to the IP. Each of them is composed of two BPM buttons. The vacuum chamber at the IP is a special design, the interaction laser needs to be able to enter and exit the chamber in order to produce X-rays via Compton interaction with the electron beam. Two windows have then been cut in the curved sections of the IP chamber which contributes to the machine impedance. As it is not possible to simulate curved section in CST, the same windows have been adapted to a straight line geometry similar to the one of the IP chamber to estimate the wakefield generated.

2.3. Pumping ports

ThomX pumping ports consist of a circular opening in the vertical plane behind a grid which continues ThomX typical cross section. There are several types of pumping ports in the storage ring, some of them in bent regions. The bent pumping port impedance is assumed to be the same as the ones in straight sections. As for the bellows, the pumping port impedance is of the broad band type, with a very low amplitude at the lower frequencies but the amplitude slowly increases at higher frequencies. Around 50 GHz, the bellows, the pumping ports and the BPMs account for more than 50 % of the total broad band impedance.

2.4. Kickers

Kickers are often complex pieces to handle with respect to impedance estimation, as shown by the high number of publications focusing on kicker impedance evaluation. ThomX kickers are composed of an elliptic ceramic chamber which is coated by a thin ($\approx 100\,\mathrm{nm}$) layer of titanium which is partially oxidised on surface due to the air contact during the manufacturing process. The chamber has to allow the magnetic field, produced by the fast kicker magnets, to go inside the chamber for the kicker to be effective which is why the ceramic is used as the body of the chamber. In the same time, the chamber is coated by a conductor in order to allow the image current to flow along the coating and limit heating and wakefield emission.

But having a ceramic chamber also mean than the beam electromagnetic field can reach outside of the chamber and can interact with outside materials. In particular, the magnet system is composed of rectangular ferrite yokes. The interaction of the beam electromagnetic field with the ferrite is a concern as it is known to produce high impedance for past kickers [20, 21, 22]. But this type of element, with thin coatings and ferrite, is very complex to simulate on software like CST because the huge number of mesh cells needed to take into account the different scales. Even with adaptive mesh cells, the 3D model would still need more than 10^9 mesh cells in order to correctly model both the thin coating and the rest of the structure. An eventual simulation this way would take much more memory and computation time than what is affordable.

So to evaluate the kicker impedance, an analytical model close to the kicker geometry and allowing to tackle the issues raised was used: the multi-layered cylindrical chamber model [23] computed using IW2D [24]. This model allows to derive the impedance of a 2D (i.e. infinite in the longitudinal direction) axisymmetric structure composed of different circular layers. This model is very well adapted to the ceramic chamber, as the ceramic and the coatings have uniform width (supposedly for the titanium and its oxidised part) corresponding well to a layered model. For the magnet system part, which is further from the beam, its geometry is neither axisymmetric nor uniform but it will be approximated

as so. The elliptic geometry of ThomX kickers has been taken into account using Yokoya factors to correct the results given for a circular geometry [25]. Compared to simulations, the advantage of using an analytical model is that it is very easy to get the impedance up to very high frequency, up to 1 THz for this study.

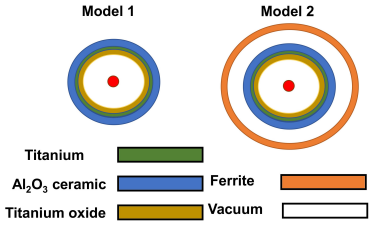

Figure 3: Models used in IW2D based on ThomX kicker geometry. The parameter used for the materials are shown in Table 3.

Table 3: Parameter used in IW2D for ThomX kicker materials: ρ_{DC} is the DC resistivity of the layer, τ is the resistivity relaxation time, ϵ_b is the real part of the dielectric constant, χ_m is the magnetic susceptibility, f_m is the permeability relaxation frequency and h is the layer thickness.

Material	ρ_{DC} (Ω m)	τ (s)	ϵ_b	χ_m	f_m (Hz)	h (m)
Titanium oxide TiO_2	10^{13} (10^{11} to 10^{15})	0	1	0	∞	10×10^{-9}
Titanium Ti	5.5×10^{-7}	$5.7 \times 10^{-16} \approx 0$	1	0	∞	90×10^{-9}
Aluminium oxide Al_2O_3	10^{12}	0	9.8	0	∞	5×10^{-3}
Ferrite	10^{6}	0	1	2000	∞	15×10^{-3}

Using IW2D, several layered models were used to design a more realistic kicker model, see Fig. 3. The first model is composed of layers of vacuum, titanium oxide, titanium and then of alumina ceramic. The second one has two additional layers, a vacuum layer followed by a ferrite layer. The model 1 is used to cover the two kicker extremities where there is no ferrite and the model 2 is used for the central part which houses the magnet system. The

longitudinal impedance produced by this realistic kicker model is shown in Fig. 4. The impedance spectrum is composed of an important broad band component with oscillations with a period of 10 GHz. The large value of the broad band maximum is due to the bad conductivity of both the ceramic and the titanium oxide. The oscillations are linked to the high dielectric constant, $\epsilon_b = 9.8$, of the ceramic. The high magnetic susceptibility of the ferrite, $\chi_m \approx 2000$, leads to the high frequency impedance oscillations seen on the spectrum and on the high amplitude resonance at 58 GHz.

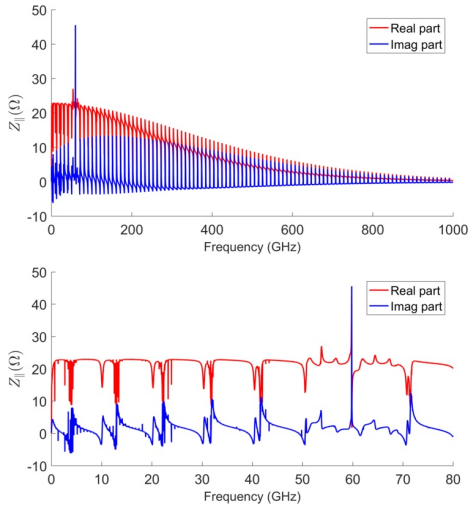

Figure 4: Longitudinal impedance produced by the kicker versus frequency. Real part is in red and imaginary part in blue. The top plot is the full spectrum from DC to 1 THz and the bottom one is a zoom ranging from DC to 80 GHz. This results corresponds to 126 mm of model 1 and 204 mm of model 2.

Several approximations were made to obtain the kicker impedance. The actual geometry of the magnet system is neglected, some physical parameters of the materials (i.e. χ_m) are known to be frequency dependent but not considered as such in this model and the value of most of the parameters is subject to large uncertainties. The value of χ_m for the ferrite layer which has been used is the DC value, which should lead to overestimate the impedance (χ_m is supposed to decrease with f). In order to estimate the error due to large parameter uncertainties, the models 1 and 2 composing the final kicker model have been

computed for different parameters within their probable range. Overall, the error ΔZ due to the lack of knowledge about material parameter should be $\Delta Z \approx \pm\, 5\,\Omega$. This corresponds to a 20 % error on the estimation of the loss factor $k_{\|}$ for the kickers.

2.5. Septum, transverse feedback (FBT) and RF cavity

The septum chamber is designed to allow the beam injection and extraction while shielding the stored beam from the septum DC magnet. The main body of the chamber is shielded from the constant magnetic field produced by the septum magnet with a thin layer of mu-metal. Mu-metal is metal with an high relative magnetic permeability μ_r which prevent the DC component of the magnetic field to go through it. Thanks to this mu-metal layer, the stored beam is not affected by the septum magnet magnetic field.

The septum chamber is a complex piece with respect to impedance estimation because it presents many different features impacting the impedance. Firstly, the septum chamber begins with a taper transition from the ThomX cross section to a rectangular cross section. Then, this rectangular cross section is reduced in the horizontal plane to allow for the injection/extraction windows, this transition corresponds to a step in and then to a step out in the horizontal plane. Finally, the central part shows both a pumping grid on one side and the mu-metal shield all around this central region. The mu-metal magnetic permeability is highly frequency dependant, $\mu_r = 520 \times 10^3$ at DC and $\mu_r = 80 \times 10^3$ at 60 Hz. It is possible to use frequency dependant materials in CST, but in practice the computational cost explodes when trying to use it to model thin layers for a high frequency range. So, as it is known that the magnetic permeability of the mu-metal decreases very quickly with frequency [26], the relative magnetic permeability of the mu-metal has been set to 1 in the wakefield simulations. The impedance found for the septum is broad band and very characteristic of a step transition with a frequency cut-off around 5.5 GHz.

The transverse feedback (FBT) aims to damp the injection jitter and to suppress transverse instabilities. It uses a stripline kicker composed of four

electrodes, which reproduces ThomX cross section, connected to electrical feed-through at both ends. The electrodes are supported by ceramic (marcor) holders and are connected to the feed-through via coper foils. In order to minimise the impedance, 0.5 mm capacitive gaps have been added on each side of the electrodes. This capacitive gap, combined with the inductance of the feedthroughs and copper foils, and the 50 Ω electric impedance of the electrodes, creates a low pass filter [27]. The cut-off frequency of this filter depends on the height of the capacitive section h. CST simulations have been done for several values of the height of the capacitive section h, varying h from 0 mm to 15 mm, in order to find the value that would minimise the impedance. The design with $h = 10\,\mathrm{mm}$ is chosen as it allows to reduce the loss factor from $k_{\parallel,h=0mm} = 0.21\,\mathrm{V\,pC^{-1}}$ to $k_{\parallel,h=10mm} = 0.15\,\mathrm{V\,pC^{-1}}$ for a $\sigma_z = 2\,\mathrm{mm}$ bunch length.

The RF cavity used in ThomX is a 500 MHz single cell copper cavity of the ELETTRA type [28], tapers are used to adjust its cross section to ThomX vacuum chamber one. As time domain wakefield simulations are not well adapted to compute the impedance of an RF cavity, the cavity has been simulated in the frequency domain. The longitudinal and transverse modes of the cavity have been simulated with eigenmode solvers and measured using a vector network analyser (VNA) in transmission mode [29]. The impedance of the RF cavity can then be built using the RLC resonator model [30]. The RF cavity contribution to the total impedance is not shown in Fig. 1 as its impedance only corresponds to very high amplitude, narrow resonances. The tapers have been simulated in CST and their impedance is broad band with a frequency cut-off around 10 GHz. The value indicated in Table 2 corresponds to the loss factor of both the RF cavity and its tapers simulated together, $k_{\parallel,RF+tapers} = 3.14\,\mathrm{V\,pC^{-1}}$, which is superior to the sum of the loss factor of its two components taken individually $k_{\parallel,RF} + k_{\parallel,tapers} \approx 2.97\,\mathrm{V\,pC^{-1}}$.

3. Impedance measurements using the coaxial wire method

Impedance evaluation is not always a straightforward affair, using analytical models provide an exact solution but the model seldom corresponds to the real

object one wants to evaluate. Nowadays, electromagnetic simulations are very powerful and perfected tools but this often come with an increased difficulty to set the numerous parameters of these "black boxes" like solvers. Because of this difficulty to parameter, it is possible to get a simulation result far from reality if the simulation is incorrectly set. RF measurements have the advantage to allow the component direct measurement, contrary to analytical models and simulations where a model has to be set. But the measurement is difficult, not always easy to interpret and is not possible for every elements. Finally, beam measurements of the impedance allow the accuracy of an existing impedance model to be checked. But, in most cases, it comes too late in the process to allow for the element modification if too big an impedance is detected.

For these reasons, when building an impedance model for a machine, common wisdom says that, ideally, one should use at least two different methods for each element one wants to evaluate. In order to constitute ThomX impedance model, the main method which was chosen is time domain simulation using CST. Then, when possible, RF measurements were done in order to cross check the simulation results. This section describes the impedance measurements done using the coaxial wire method. It first focuses on the setup used and on the measurement limitations, the measurement of the bellows with and without RF fingers, see Fig. 2, is then presented and compared with simulations.

3.1. Measurement setup

Impedance measurements using the classical coaxial wire method use the fact that electromagnetic field produced by an ultrarelativistic beam is close to the one produced by a coaxial TEM transmission line [31]. It is then possible to measure the impedance using a Vector Network Analyser (VNA) matched to the TEM transmission line created by a Device Under Test (DUT) and a wire inserted inside the DUT. The VNA measures the transmission parameter $S21$, which corresponds to the ratio of the output power wave to the input power wave. The measurement of the DUT is carried out with respect to an ideal reference line in order to remove any effect coming from the setup. The principle

of the measurement is described in more detail in [12, 13]. The log-formula has been chosen for the impedance evaluation from the RF measurements [32]:

$$Z = 2Z_L \ln\left(\frac{S21_{DUT}}{S21_{REF}}\right) \tag{1}$$

where Z_L is the line impedance of the DUT. The log-formula has the advantage of being able to correctly resolve lumped impedance parts while keeping an acceptable error for distributed impedance parts [12].

The measurement setup is presented in Fig. 5. A half shell flange is used to support the measurement setup, an RF bulkhead going through the half shell links the cable going to the VNA (Vector Network Analyser) to the RF connector. A coaxial cable brazed on the RF connector and stripped on the end tip is used as an antenna. A resistor is brazed on the stripped tip of this coaxial cable in order to match the two coaxial lines. Then the CuBe (Copper Beryllium) wire is brazed on the other end of the resistor. A metallic plate is used to separate the RF connector part from the measurement part. If there is no separation then the TEM modes created between the external conductor of the coaxial conductor can propagate and disrupt the measurement. In order to damp reflections on this plate, RF absorbing foam has been glued to it. In the aim of improving repeatability, the plate and the foam have been glued to a metallic support which can be removed to screw the RF connector and tauten the wire.

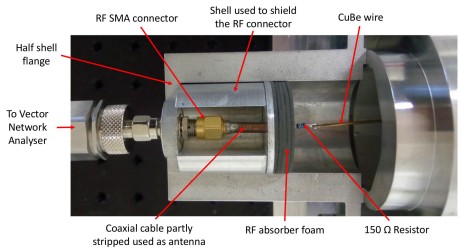

Figure 5: Measurement setup for longitudinal impedance using the coaxial wire method

A TEM coaxial line is created by the wire going trough the vacuum chamber. In order for the electromagnetic wave from the VNA to propagate without

reflections to the system along the wire, the two lines $Z_0 = 50\ \Omega$ and Z_L must be adapted by a matching resistor [13].

The line impedance Z_L of a ThomX beam pipe has been simulated using CST^{TM} MW for different wire diameters and compared with the analytic formula for the case of round chambers. In this case, it is necessary to determine an equivalent diameter D_{eq} for ThomX cross section which is not cylindrical. The value of this equivalent diameter $D_{eq} = 30.9$ mm is chosen so that the analytical results match the simulations. The material of the wire is chosen to be copper beryllium (CuBe) in order to be able to tauten the wire without stretching it. The half shell flanges have been designed to have a diameter of $D_{eq} = 30.9$ mm to have the same line impedance Z_L as the vacuum pipe one.

In order to be able to measure high impedance components, it is important to have the highest line impedance Z_L possible [13]. Ideally the line impedance should be much higher than the DUT impedance. However, there is a compromise to be made between the frequency precision and attenuation of the signal with respect to the wire diameter which will be explain briefly in the measurements section [33, 34]. Firstly, we started to do measurements with a wire diameter of $d = 1$ mm which gives a line impedance of $Z_L = 205.7 \pm 6.0$ Ω.In this case, the matching is done using a resistor of $R_s = Z_L - Z_0 \approx 150\ \Omega$. To compare the impact of wire thickness, the measurements were also done with thinner wires of 0.1 mm and of 0.025 mm. Using thinner wires increase the line impedance Z_L and allow for a better precision when measuring high impedance components. These additional measurements will also help to determine the influence of the wire diameter on the signal attenuation. The line impedance corresponding to the 0.1 mm and 0.025 mm wires were calculated with respect to analytic formula and they are equal to 343.76 Ω and 426.88 Ω respectively [13].

3.2. Measurement limitations

The coaxial wire measurement of the impedance has many limitations which can prevent a good measurement. Some limitations come from the setup and

other come from the method used to do the measurement.

A first limitation is fixed by the calibration done on the VNA before doing the measurement. Using a calibration kit valid down to -40 dB it is not possible to accurately measure below -40 dB. This means that, using Eq. (1), the maximum impedance value which can be precisely measured using this setup is $Z_{max} = -2Z_L \ln(-40dB) \approx 1900\ \Omega$ with 1 mm wire. This limit is further reduced because the measurement of the reference has to be taken into account.

A second limitation would be due to the repeatability of the measurements. When doing coaxial wire measurements many aspects change from measurement to measurement and may increase the uncertainty of the measurement: the brazing and the tautening of the wire, the positioning of the RF absorbing foam, the screwing of the half shell flanges on the DUT, ... In order to decrease the statistical errors, several measurements have been taken and the impedance is computed from the averaged value. Systematic errors include the effect of the wire thickness and the limitations of the log-formula. A support to fix the positioning of the RF foam is used and the measurement is done in a clean room with fixed temperature and pressure. A precise error quantification has been done to estimate this limitation, see Appendix A.

Lastly the coaxial wire method has been shown to be inaccurate below the beam pipe cut-off frequency [35]. The stretched wire perturb the behaviour of the electromagnetic field by allowing TEM waves with zero cut-off frequencies whereas, in realistic situation with a beam, these modes would not be able to propagate. The cut-off frequency (TE_{11}) for a round pipe is given by $f_c = \frac{j_{1,1}c}{2\pi R}$ with $j_{1,1}$ the first root of the Bessel function J_1, c the speed of light and R the radius of the beam pipe. For ThomX cross section, if the value $R_{eq} = \frac{D_{eq}}{2}$ is used then, $f_c = 5.7$ GHz. The method is known to give good results above 30 % of the cut-off [35], for ThomX this would mean above $1.3 f_c \approx 7.4$ GHz. Below 7.4 GHz, the amplitude and frequency shift introduced by the wire can be seen as an additional error on the measurement.

As the limitations are severe, in our case the coaxial wire method is only used to validate the simulation tools and methods.

3.3. Measurement of the reference section

In order to measure impedance by the wire method, it is necessary to measure an "ideal reference line" corresponding to $S21_{REF}$ in Eq. (1). This measurement is used as the reference to take into account the defaults of the setup and the particular geometry of the beam pipe cross section. The reference section used here is a plain vacuum pipe using ThomX cross section. Ideally, the reference section and the DUT should have the same length. But in our case, there are many objects of different length to measure and it does not seem justified to make new reference sections for each object to measure.

Two length of reference section were measured, 100 mm and 500 mm. The two $S21$ measurements give very similar results but the longer section shows small oscillations on top of the general behaviour shown by both sections. As the difference between two sections of very different length is small enough, it is legitimate to use one of these two measurement as reference for a DUT no matter its length. For smaller DUT, which size is around 100 mm, the smaller one is used and for bigger DUT the other is used.The comparison of the 100 mm and 500 mm can be seen in Fig.6.

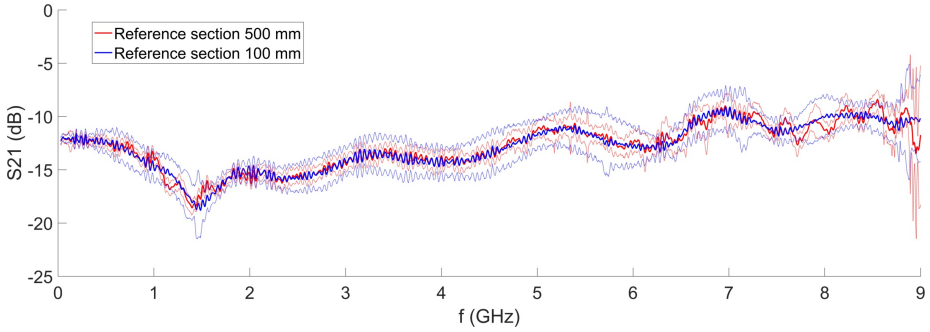

Figure 6: S21 measurement of ThomX reference section, the 100 mm section is plotted in blue and the 500 mm section in red. The mean value for the set of 5 measurements is plotted in plain line and the 95 % CI is shown in dotted lines.

3.4. Measurements

The RF measurement of the bellows has been done with and without the RF fingers to test the effectiveness of the RF fingers in suppressing the trapped

modes. The transmission parameter $S21$ for these measurements is shown in Fig. 7. The measurement of bellows with RF fingers is very close to the reference measurement which indicates that the shielding works as intended. The measurement without RF fingers shows strong resonance peaks which clearly stand out of the reference measurement.

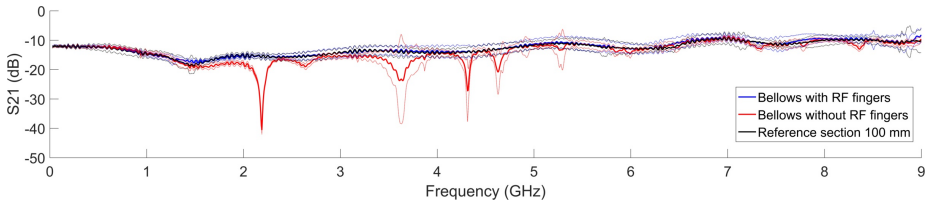

Figure 7: S21 measurement of ThomX bellows, with RF fingers in blue, without RF fingers in red and the 100 mm reference section in black. The mean value for the set of 5 measurements is plotted in plain line and the 95 % CI is shown in dotted lines.

Figure 8 shows the real part of the impedance obtained using the log formula, Eq. (1). It is compared with CST simulations of the impedance for both cases, in dotted lines with RF fingers for the top plot and without RF fingers for the bottom plot for the 1 mm diameter wire.For the bellows with RF fingers, the measurement agrees very well with the simulation which gives a very low impedance.

For the bellows without RF fingers, firstly the measurements were done with 1 mm wire. The simulation agrees relatively well with the measurement as the four peaks found in simulation also appears in the measurement. The two strong peaks at 2.1 GHz and 3.5 GHz in the simulation are shifted respectively at 2.2 GHz and 3.6 GHz in the measurement and have a lower amplitude value by a factor 8 to 10. The two smaller peaks at 4.4 GHz and 4.8 GHz are shifted respectively at 4.3 GHz and 4.6 GHz but have comparable amplitude. The differences in amplitude and the shifts in frequency can be explained by the variable geometry of a real bellows compared to the fixed bellows modelled in CST simulation, the loss in the resistors and the attenuation due to the thickness of the wire [36]. For example, the resistors used for line impedance matching can bring additional noise for high frequency applications. The current density

is related to frequency for resistor which creates additional noise and power loss [34]. For comparison, the same measurements were done with the thinner wire of 0.1 mm. The reproducibility error with 0.1 mm wire on the bellow and reference section measurements were reduced nearly half compared to the 1 mm wire measurements and even more in the case of the high resonance peaks as it can be seen in Figure 9. The most likely reason is the change in the wire tension coming from the difficulty in stretching the 1 mm wire. With the 0.1 mm wire, the frequency shift with respect to the impedance calculations was reduced significantly as it can be seen in Figure 10 however the attenuation gets bigger with the thinner wire [36]. Also the strong field distortion due to the insertion of the wire creates frequency shifts in impedance spectrum decreasing when the wire diameter gets smaller [33, 34]. In the measurement, the peaks are broader than in the simulations as all the components of the real bellows do not resonate at the same frequency due to small variations in the bellows period which do not exist in the perfect model used for simulations. As a good trade off between the frequency precision and the attenuation, it was decided to use 0.1 mm wire for future measurements. It is important to note the effectiveness of the RF fingers in suppressing the high impedance measured without the RF fingers.

In addition to the bellows, measurements have also been performed on several prototypes of BPMs, of pumping ports and of the RF cavity and its tapers [8, 29]. Despite the important uncertainty and the limited frequency range of the measurements, they have allowed to check that the elements were correctly represented in CST, and that the element design and manufacture is suited to produce low impedance elements.

4. Coherent synchrotron radiation impedance model using CSRZ

In this section, a coherent synchrotron radiation (CSR) impedance model for ThomX storage ring is developed following the same idea as for the geometric and resistive wall impedance. The CSR community usually uses a different convention for the impedance and the wake functions compared to the one use

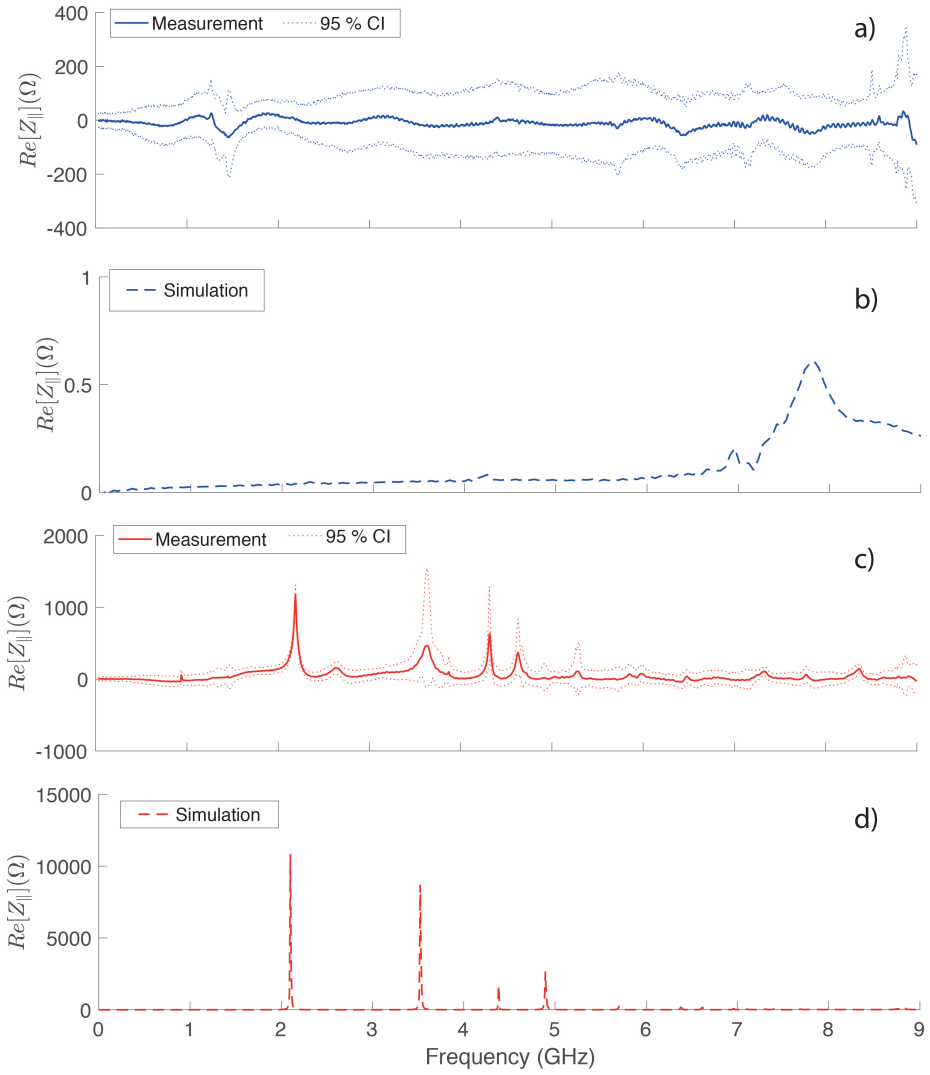

Figure 8: Real part of the impedance of ThomX bellows : a) Measurement with RF fingers, b) Simulations with RF fingers, c) Measurements without RF fingers, d) Simulations with RF fingers. The mean value for the set of 5 measurements is plotted in plain line and the 95 % CI is shown in thin dotted lines for a) and c).

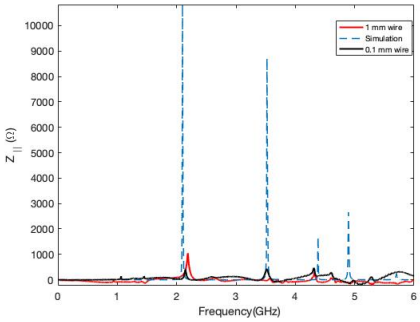

Figure 9: The real part of the simulated and measured impedances for 1 mm and 0.1 mm wire

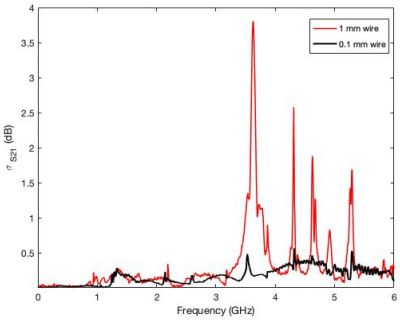

Figure 10: The standard deviation on the bellow measurements for 1 mm and 0.1 mm wire

here and used in the literature for the geometric and resistive wall wakefields [15, 30, 37]. In the CSR convention, a positive wake function corresponds to an energy loss and the impedance spectrum is the complex conjugate of the one use here. This section keeps using the same convention used in this paper but plots $-Im[Z]$ in the impedance spectrum in order to keep the usual display of the impedance for the CSR.

The steady-state parallel plate model is often used to estimate the CSR impedance [38, 39, 40]. In this model, an electron (point like charge) moves in between two perfectly conducting plates separated by a distance h on the horizontal direction. As it takes into account the shielding created by the beam pipe walls, this model adds a threshold f_{sh} below which the CSR impedance is very strongly reduced compared to the free space model [38, 39].

These simple models correspond to a steady-state situation where the electron bunch trajectory is perfectly circular. In most real machines, the dipoles are interleaved with drift spaces which introduce transient effects at dipole entrance and exit. The CSR fields emitted in the dipoles are guided by the vacuum chamber, acting as a waveguide, and propagate along the beam in the straight sections, see (c) of Fig. 11. This effect, also called "drift CSR", is more important if the machine contains short dipole magnets. Some more complicated analytical models take into account transient effects [41, 42].

In addition to transient effects, the CSR fields can also be reflected, sometimes multiple times, on the transverse beam pipe walls, as in (b) of Fig. 11. The reflections on the outer walls lead to head-tail effects while the reflections on the inner walls lead to tail-head effects. When the magnet is long compared to the vacuum chamber width a, the CSR fields can resonate within the vacuum chamber and excite the eigenmodes of the vacuum chamber [14]. Furthermore, the CSR fields radiated in a dipole can propagate until the next dipole and interfere with the new CSR fields produced in this second dipole [14].

For now, the only way to consider all these effects is to use numerical methods which allow to simulate the CSR wakefield or CSR impedance for a given beamline and vacuum chamber geometry. The CSRZ code, by Demin Zhou, is a

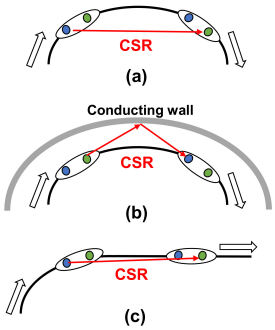

Figure 11: Schematics of the electron interaction within a bunch due to coherent synchrotron radiation (CSR). White arrows show the propagation direction of the bunch and red arrows the emitted CSR field. The bunch is represented by an ellipse with the black contour with inside an electron of the tail in blue and one of the head in green. (a): effect of CSR in free space, the CSR radiated by the tail affects the head of the bunch. (b): effect of the walls, the CSR radiated by the head is reflected on the walls and affects the tail. (c): transient effect at dipole exit, the CSR field emitted at the dipole exit travels parallel to the bunch and interacts with it during the drift.

FORTRAN 90 code which allows to compute the CSR impedance of a beam by numerical integration of Maxwell's equations in the paraxial approximation [14, 43]. The code considers a beam pipe of constant rectangular cross section with a curvature defined by an arbitrary function of the longitudinal coordinate s. It brings the possibility to simulate CSR with the real disposition of the dipole magnets in a lattice. The code assumes a constant Gaussian bunch in every dimensions. After the geometry defined by the user, an infinite straight section can be added to integrate the CSR fields produced in bends and can take into account additional transient effects.

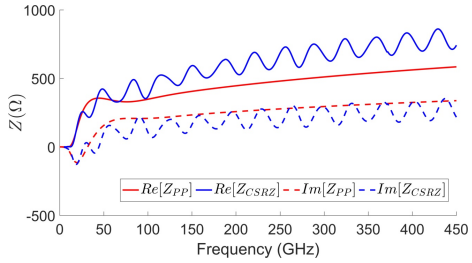

Figure 12: CSR impedance computed with the parallel plate model Z_{PP} (steady-state) in red and using CSRZ for a single ThomX ring dipole Z_{CSRZ}. The real part of the impedance is shown in plain lines and the imaginary part in dotted lines. Parameters: $L = 0.2964\,\mathrm{m}$, $R = 0.3773\,\mathrm{m}$, $h = 28\,\mathrm{mm}$, $a = 40\,\mathrm{mm}$.

A ThomX storage ring dipole has been simulated using CSRZ, approximating ThomX vacuum chamber with a beam pipe of rectangular cross section with an horizontal dimension of $a = 40\,\text{mm}$ and a vertical one of $h = 28\,\text{mm}$. In figure 12, the CSR impedance computed with CSRZ for a single bend in ThomX, Z_{CSRZ}, is compared to the CSR impedance computed using the parallel plate model Z_{PP}. Both the analytic model and the numerical calculation agree on the frequency value for the CSR threshold, around 11 GHz. Compared to the very smooth impedance of the parallel plate model, the impedance computed using CSRZ shows oscillations corresponding to the resonances of the CSR fields within the rectangular vacuum chamber both in the real and in the imaginary part. The amplitude difference between the curves is due to the transient effects which increase the amplitude of the real part and decrease the one of the imaginary part.

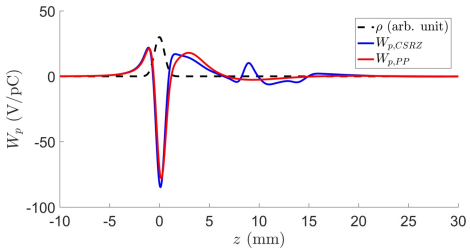

Figure 13: CSR wake potential radiated by a Gaussian longitudinal charge density ρ ($\sigma_z = 0.5\,\text{mm}$) for a ThomX ring dipole with the parallel plate model $W_{p,PP}$ and with CSRZ $W_{p,CSRZ}$. The head of the bunch corresponds to negative z values and the tail to positive z values.

The wake potential $W_{p,CSRZ}$ generated by the Z_{CSRZ} impedance spectrum for a Gaussian bunch of $\sigma_z = 0.5\,\text{mm}$ is shown in Fig. 13. It is compared to the wake potential of the parallel plate model $W_{p,PP}$, the amplitude of $W_{p,CSRZ}$ is slightly more important due to the transient effects. The $z < 0$ zone is similar for the two wake potentials, which means that the tail-head interaction is not affected by the inner walls of the vacuum chamber in this case. The $z > 0$ zone is modified compared to the parallel plate case, with a longer wake trailing behind the bunch. This change is brought by the effect of the outer walls, bringing an additional head-tail interaction, and the resonances within the vacuum chamber.

The CSRZ simulation has also been performed for multiple bends in order to estimate the effect of the CSR field interference [8]. The interference between the CSR emitted in each bend produces additional oscillations on the real part and imaginary part of the impedance which are amplified as more and more dipoles are added. For the full ring, the impedance spectrum is full of resonant peaks but keeps the same mean amplitude as Z_{CSRZ}. Unfortunately, this computation is very long, several months of calculation for the full ThomX 18 m ring with a frequency step thin enough to resolve properly these peaks in the impedance spectrum.

5. Summary and conclusion

An impedance model, for both the geometric wakefields and the coherent synchrotron radiantion (CSR), has been designed for the particular case of ThomX [2, 3], a laser-electron storage rings [1] for X-ray production via Compton backscattering.

The geometric and resistive wall impedance model designed is based on simulations of every elements of the storage ring. Then the coaxial wire method has been used to measure prototypes of the storage ring elements to check the simulations. A precise evaluation of the different error sources of these measurements has been done and highlights the important uncertainty of this type of measurements. Nevertheless, the measurements have allowed to validate the simulations. As the simulation of the kicker impedance was not possible, because of very thin coatings, an analytical model, the multi-layered cylindrical chamber [23], has been used to evaluate the kicker impedance. The total impedance budget has been presented, corresponding to a loss factor of $k_{\parallel,T} = 6.73\,\mathrm{V\,pC^{-1}}$ for a Gaussian bunch of $\sigma = 2\,\mathrm{mm}$. To this value, the RF cavity and its tapers contribute for 47 %, the septum chamber for 17 %, the kickers for 12 % and the rest is distributed among the other components of ThomX storage ring.

The CSR impedance model has been obtained by simulation of the beam in a rectangular vacuum chamber. It has allowed to take into account transient

effects, due to straight sections in between dipoles, and resonances, due to reflections on the beam pipe, using the CSRZ code [14, 43]. The result has been compared with the parallel plate model and has shown the importance of the transient effects and resonances in ThomX dipoles.

These impedance models have been used to extract pseudo wake functions which are used to feed the codes currently used for ThomX beam dynamics studies. The analysis of these two models provide important insight on the influence of collective effects in ThomX beam dynamics. The quantity $Re[Z]|\tilde{\rho}|$ is related to the total energy loss of a bunch of spectrum $\tilde{\rho}$ due to the impedance Z [30]. This quantity is shown for both impedance models for a short bunch, $\sigma_s = 2\,\mathrm{mm}$ $= 6.6\,\mathrm{ps}$, and for a longer bunch, $\sigma_s = 6\,\mathrm{mm} = 20\,\mathrm{ps}$, in Fig. 14. At injection, the bunch corresponds to the short bunch case, for which the dominant effect is the CSR. After some time, the bunch has fully filled the RF bucket due to the filamentation induced by the longitudinal mismatch at injection. For the long bunch obtained, the effect of the CSR is small compared to the geometric and resistive wall wakefields. It confirms that, in ThomX case, simulating the geometric impedance up to 50 GHz is enough. As, for short bunches for which high frequencies are important, the CSR is the dominant effect. This simple analysis also highlights two distinct regimes for the longitudinal dynamics. A transient regime during which the CSR has a strong impact due both to the injection of a short bunch and to the filamentation [8]. And another regime, which starts after the emittance dilution, which corresponds to the classic potential-well distortion.

Acknowledgments

The authors would like to thanks David Amorim, Nicoló Biancacci, Elias Metral, Benoit Salvant and the CERN impedance team for their advice at the start of this studies and for providing the IW2D code. The authors also would like to thanks Demin Zhou for providing the CSRZ code and for his help and advice on how to use his code. Moussa El Ajjouri is also thanked for his help on the FBT and BPM impedance evalution. Clément Evain, Alexandre Loulergue

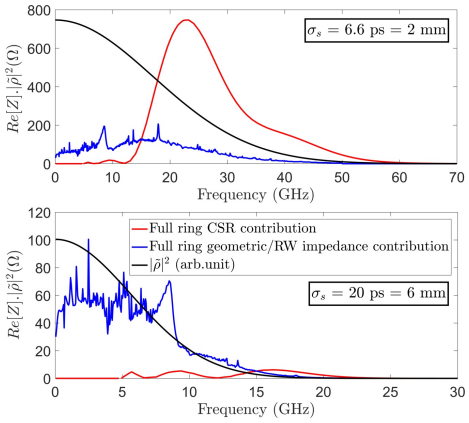

Figure 14: Plots of the product $Re[Z]|\tilde{\rho}|^2$ versus the frequency for different bunch length σ_z. The impedance Z corresponds to the CSR impedance of the full storage ring for the red line ($8 \times Z_{CSRZ}$, see Fig. 12). The impedance Z corresponds to the full geometric/RW impedance model, see Fig. 1, for the blue line. The black line shows the modulus squared of the bunch spectrum $|\tilde{\rho}|^2$ is arbitrary units (arb. unit).

and Ryutaro Nagaoka are also acknowledged for fruitful discussions. Engineering office and mechanical department from LAL are thanked for the conception and the realisation of the impedance measurement bench and for the many exchanges that were needed to design ThomX impedance model. This work is supported by ANR-10-EQPX-51, by grants from Région Ile-de-France and IN2P3.

Appendix A. Errors estimate for the coaxial wire measurement

The main source of error in the impedance measurement is due to the $S21$ measurements, especially the error on the repeatability of the measurements. A bunch of 5 different measurements of each pieces measured have been done to test these bias. After each measurement, the brazing and the tautening of the wire were changed. The typical value for the standard deviation is about $\sigma_{S21} = 0.4$ dB but it increases with frequency.

As the error is inferred from a small set of repeated measurements, type A uncertainty, a Student t-distribution for the error is assumed [44]. So the standard uncertainty is given by $u_{S21_M} = \sqrt{\frac{\nu}{\nu-2}}\sigma$, with $\nu = N - 1$ degrees of

Variable (Unit)	Error source	Type	Probability distribution	Standard uncertainty u
$S21_{REF/DUT}$ (dB)	Repeatability	A	Student	$u_{S_M} = \sqrt{\frac{4}{4-2}}\sigma_{S21} \approx 0.57$ (Variable)
$S21_{REF/DUT}$ (dB)	VNA Calibration	B	Triangular	$u_{S_C} = \frac{0.2}{\sqrt{6}} \approx 0.082$
$S21_{REF/DUT}$ (dB)	VNA Resolution	B	Rectangular	$u_{S_R} = \frac{0.02}{2\sqrt{3}} \approx 0.0082$
d (mm)	Manufacturing	B	Gaussian	$u_d = 0.1$
D_{eq} (mm)	Modelization	B	Gaussian	$u_D = 0.1$

Table A.4: Sources of errors for impedance measurements. The standard uncertainty for the repeatability of $S21_{REF/DUT}$ is computed for $\sigma_{S21} = 0.4$ dB

freedom, N the number of measurement in a set and σ the standard deviation of the measurement set.

Other sources of errors, type B uncertainty, for the $S21$ measurement are the VNA resolution limit and calibration. The VNA used to do the measurement is an Anritsu MS4624B, last calibration check in a metrology laboratory shown a maximum error of $e = 0.2$ dB (at -50 dB) when compared to a reference. A triangular distribution of the errors is assumed as this value e is the maximum error and not the most probable error. The resolution limit of the VNA is $r = 0.02$ dB at maximum. In this case a rectangular distribution of the errors is assumed as all values v are equally likely in $\left[v - \frac{r}{2}, v + \frac{r}{2}\right]$.

In addition to the error on the $S21$ measurement there is also an error on the determination of the line impedance Z_L. The error on the wire diameter d is given by the manufacturer $u_d = 0.1$ mm. The error for ThomX equivalent diameter D_{eq} is the fitting error which is about $u_D = 0.1$ mm. Table A.4 shows the summary of the different error components, their sources and their respective probability distribution.

Using uncertainty propagation on Eq. (1) gives the composed standard un-

certainty of the impedance measurement u_Z in Eq. (A.1) [44]. The standard uncertainty on the $S21$ measurement u_S is given by: $u_S = u_{S_M} + u_{S_C} + u_{S_R}$. With u_{S_C} the standard uncertainty on the calibration, u_{S_R} the standard uncertainty on the resolution. The standard uncertainty on the repeatability of the measurement u_{S_M} depends on the object measured and on the frequency considered.

$$u_Z = \frac{Z_v}{\pi} \sqrt{\ln^2\left(\frac{S21_{DUT}}{S21_{REF}}\right)\left(\frac{{u_D}^2}{D^2} + \frac{{u_d}^2}{d^2}\right) + \ln^2\left(\frac{D}{d}\right)\left(\frac{{u_{S_{DUT}}}^2}{{S21_{DUT}}^2} + \frac{{u_{S_{REF}}}^2}{{S21_{REF}}^2}\right)} \tag{A.1}$$

But Eq. (A.1) is not usable in this state as when using uncertainty propagation formulas the standard uncertainties u_S should be absolute uncertainty. As it is shown in Eq. (A.2) to Eq. (A.4), the absolute uncertainties in dB (with index dB) change into relative uncertainties when changed back in linear scale (with index L). Furthermore the transformation from dB scale to linear scale leads to an asymmetry of the uncertainty boundaries.

$$S21_{dB} - u_{S_{dB}} < S21_{dB} < S21_{dB} + u_{S_{dB}} \tag{A.2}$$

$$\frac{S21_L}{u_{S_L}} < S21_L < S21_L u_{S_L} \tag{A.3}$$

$$S21_L + S21_L(\frac{1}{u_{S_L}} - 1) < S21_L < S21_L + S21_L(u_{S_L} - 1) \tag{A.4}$$

Finally Eq. (A.5) is obtained, in which all the quantities are in linear scale, and gives the upper and lower composed standard uncertainties. For example if the transmission parameter S21 for the reference is measured at -10 dB, for the DUT at -15 dB and that both measurements have a standard deviation of $\sigma_{S21} = 0.4$ dB at this frequency point then the impedance measured is $Z = 237^{+49}_{-46}\ \Omega$. In that case, 98 % of the uncertainty on the impedance is due to the uncertainty on S21 measurements and 2 % on the line impedance Z_L.

$$u_Z^{\pm} = \frac{Z_v}{\pi} \sqrt{\ln^2\left(\frac{S21_{DUT}}{S21_{REF}}\right)\left(\frac{{u_D}^2}{D^2} + \frac{{u_d}^2}{d^2}\right) + \ln^2\left(\frac{D}{d}\right)\left({u_{DUT}^{\pm}}^2 + {u_{REF}^{\pm}}^2\right)} \tag{A.5}$$

$$u^+ = u_{S_L} - 1 \tag{A.6}$$

$$u^- = \frac{1}{u_{S_L}} - 1 \tag{A.7}$$

All measurement results are shown with their 95 % confidence interval (CI) corresponding to the extended uncertainty using Student coefficient $k = 2.78$ ($N = 5$). In the case of the previous example, the extended uncertainties to 95 % CI gives $Z = 237^{+137}_{-127}$ Ω. The important uncertainty found comfort us in the idea that this measurement should only be used to validate the simulation tools and methods.

References

[1] Z. Huang, R. D. Ruth, Laser-electron storage ring, Physical review letters 80 (5) (1998) 976 (1998). doi:10.1103/PhysRevLett.80.976.

[2] A. Variola, J. Haissinski, A. Loulergue, F. Zomer, others, ThomX Technical Design Report, Tech. rep., LAL (2014).
URL `http://hal.in2p3.fr/in2p3-00971281`

[3] C. Bruni, R. Chiche, R. Cizeron, Y. Fedala, J. Haissinski, M. Jacquet, D. Jehanno, M. Lacroix, L. Meignien, B. Mercier, B. Mouton, Y. Peinaud, C. Prevost, R. Roux, V. Soskov, A. Variola, G. Wormser, F. Zomer, P. Brunelle, M. E. Couprie, J. C. Denard, J. M. Filhol, N. Guillotin, P. Lebasque, A. Loulergue, P. Marchand, O. Marcouill©, F. Marteau, R. Nagaoka, P. Balcou, E. Cormier, M. C. Nadeau, P. Walter, N. Artemiev, R. Flaminio, C. Michel, L. Pinard, B. Sassolas, J. P. Brasile, ThomX - Conceptual Design Report, Tech. rep. (2009).
URL `http://hal.in2p3.fr/in2p3-00448278`

[4] T. Rui, W. Huang, Lattice design and beam dynamics of a storage ring for a Thomson scattering x-ray source, Physical Review Accelerators and Beams 21 (10) (2018) 100101 (2018).

[5] V. Androsov, A. Agafonov, J. Botman, E. Bulyak, I. Drebot, P. Gladkikh, V. Grevtsev, V. Ivashchenko, I. Karnaukhov, V. Lapshin, A. Lebedev,

V. Markov, N. Mocheshnikov, A. Mytsykov, F. Peev, A. Ryezayev, A. Shcherbakov, V. Skomorokhov, V. Skyrda, R. Tatchyn, Y. Telegin, V. Trotsenko, A. Zelinsky, X-ray generator based on Compton scattering, Nuclear Instruments and Methods in Physics Research Section A: Accelerators, Spectrometers, Detectors and Associated Equipment 543 (1) (2005) 58–64 (May 2005). doi:10.1016/j.nima.2005.01.114.
URL http://linkinghub.elsevier.com/retrieve/pii/S0168900205001993

[6] C. Bruni, J. Haissinski, A. Loulergue, R. Nagaoka, Electron Beam Dynamics in the 50 MeV ThomX Compact Storage Ring, in: IPAC'11, Joint Accelerator Conferences Website, 2011, pp. 715–717 (2011).
URL http://hal.in2p3.fr/in2p3-00635611

[7] M. Jacquet, C. Bruni, Analytic expressions for the angular and the spectral fluxes at Compton X-ray sources, Journal of synchrotron radiation 24 (1) (2017) 312–322 (2017).

[8] A. Gamelin, Collective effects in a transient microbunching regime and ion cloud mitigation in ThomX, PhD Thesis, Paris-Sacaly (2018).
URL http://www.theses.fr/2018SACLS276/document

[9] A. Loulergue, C. Bruni, J. Haissinski, A. Variola, M. Lacroix, M. Jore, T. Vandenberghe, Compact Ring for the ThomX-ray Source, in: 1st International Particle Accelerator Conference (IPAC 2010), Joint Accelerator Conferences Website, 2010, pp. 4650–4652 (2010).

[10] I. Drebot, Electron beam dynamics with and without Compton back scattering, Ph.D. thesis, Paris-Sud 11 (2013).
URL https://tel.archives-ouvertes.fr/tel-00920424

[11] V. Smaluk, Impedance computations and beam-based measurements: A problem of discrepancy, Nuclear Instruments and Methods in Physics Research Section A: Accelerators, Spectrometers, Detectors and Associated Equipment 888 (2018) 22–30 (2018).

[12] U. Niedermayer, L. Eidam, O. Boine-Frankenheim, Analytic modeling, simulation and interpretation of broadband beam coupling impedance bench measurements, Nuclear Instruments and Methods in Physics Research Section A: Accelerators, Spectrometers, Detectors and Associated Equipment 776 (2015) 129–143 (2015).

[13] F. Caspers, T. Kroyer, E. Gaxiola, Longitudinal and Transverse Wire Measurements for the Evaluation of Impedance Reduction Measures on the MKE Extraction Kickers, Tech. Rep. AB-Note-2007-028 (2007).
URL http://cds.cern.ch/record/1035461/files/ab-note-2007-028.pdf

[14] D. Zhou, Coherent Synchrotron Radiation and Microwave Instability in Electron Storage Rings, Ph.D. thesis, The Graduate University for Advanced Studies (2011).
URL http://inspirehep.net/record/1313669/

[15] CST Particule Studio.
URL https://www.cst.com/

[16] N. Biancacci, Improved techniques of impedance calculation and localization in particle accelerators, Ph.D. thesis, CERN (2014).
URL http://cds.cern.ch/record/1704527

[17] N. Hubert, L. Cassinari, J. C. Denard, N. Leclercq, A. Nadji, L. Nadolski, D. P©deau, The SOLEIL bpm and orbit feedback systems, in: DIPAC'07, 2007 (2007).
URL http://accelconf.web.cern.ch/AccelConf/d07/papers/tupc20.pdf

[18] R. Nagaoka, J. C. Denard, M. P. Level, Recent studies of geometric and resistive wall impedance at SOLEIL, in: EPAC'06, Edinburgh, 2006 (2006).

[19] A. Gamelin, C. Bruni, D. Radevych, Longitudinal and transverse dynamics of ions from residual gas in an electron accelerator, Physical Review Accelerators and Beams 21 (5) (May 2018).

doi:10.1103/PhysRevAccelBeams.21.054401.
URL https://link.aps.org/doi/10.1103/PhysRevAccelBeams.21.054401

[20] D. Davino, H. Hahn, Improved analytical model of the transverse coupling impedance of ferrite kicker magnets, Physical Review Special Topics-Accelerators and Beams 6 (1) (2003) 012001 (2003). doi:10.1103/PhysRevSTAB.6.012001.

[21] H. Tsutsui, L. Vos, Transverse coupling impedance of a simplified ferrite kicker magnet model, Tech. rep., CERN-LHC-Project-Note-234 (2000).
URL http://cds.cern.ch/record/691863

[22] H. Tsutsui, Some simplified models of ferrite kicker magnet for calculation of longitudinal coupling impedance, Tech. rep. (2000).
URL http://cds.cern.ch/record/426384

[23] N. Mounet, E. M©tral, Electromagnetic field created by a macroparticle in an infinitel long and axisymmetric multilayer beam pipe, Tech. Rep. CERN-BE-2009-039 (2009).
URL https://infoscience.epfl.ch/record/167122

[24] N. Mounet, ImpedanceWake2d.
URL http://impedance.web. cern.ch/impedance/Codes/ImpedanceWake2D/user_manual_todate.txt

[25] K. Yokoya, Resistive wall impedance of beam pipes of general cross section, Part. Accel. 41 (KEK-Preprint-92-196) (1993) 221–248 (1993).
URL http://inspirehep.net/record/353231/files/p221.pdf

[26] F. Thiel, Demagnetization of layered ferromagnetic structures for magnetically shielding: Frequency considerations, IEEE Transactions on magnetics 45 (12) (2009) 5307–5314 (2009). doi:10.1109/TMAG.2009.2022935.

[27] M. El Ajjouri, N. Hubert, A. Loulergue, R. Sreedharan, D. Douillet, A. Gamelin, D. Le Guidec, Design of the Transverse Feedback Kicker for

ThomX, in: IBIC'17, Barcelona, Spain, 2017 (2017).
URL http://www.jacow.org/ibic2016/papers/tupg08.pdf

[28] A. Massarotti, G. DÄôAuria, A. Fabris, C. Pasotti, C. Rossi, M. Svandrlik, Status report on the ELETTRA RF system, in: PAC'91, 1991 (1991).

[29] M. El Khaldi, I. V. Drebot, P. Lepercq, R. Marie, B. Mercier, T. Roulet, A. Variola, F. Wicek, H. D. Dias, M. D. Diop, others, Simulations and RF Measurements of the Fundamental and Higher Order Modes of the ThomX 500 MHz Cavity, in: IPAC'13, Joint Accelerator Conferences Website, 2013, pp. 2711–2713 (2013).
URL https://hal.archives-ouvertes.fr/in2p3-00823312/

[30] B. W. Zotter, S. Kheifets, Impedances and Wakes in High Energy Particle Accelerators, World Scientific, 1998 (1998).

[31] J. D. Jackson, Classical electrodynamics, John Wiley & Sons, 2012 (2012).

[32] L. S. Walling, D. E. McMurry, D. V. Neuffer, H. A. Thiessen, Transmission-line impedance measurements for an advanced hadron facility, Nuclear Instruments and Methods in Physics Research Section A: Accelerators, Spectrometers, Detectors and Associated Equipment 281 (3) (1989) 433–447 (1989).

[33] B. Salvant, D. Amorim, S. Antipov, S. Arsenyev, M. Beck, N. Biancacci, O. Brüning, E. Carideo, J. Campelo, F. Caspers, A. Farricker, A. Grudiev, T. Kaltenbacher, E. Koukovini-Platia, P. Kramer, A. Lasheen, E. Métral, M. Migliorati, N. Mounet, G. sur Yvette, Building the impedance model of a real machine, 2019 (05 2019). doi:10.18429/JACoW-IPAC2019-WEYPLS1.

[34] W. H. Hayt, Engineering Electromagnetics, McGraw-Hill, 1989 (1989).

[35] M. Masullo, V. Vaccaro, M. Panniello, others, The stretched wire method: A comparative analysis performed by means of the mode matching

technique, in: LINAC'10, Vol. 10, 2010, p. 159 (2010).
URL http://accelconf.web.cern.ch/AccelConf/LINAC2010/papers/thp081.pdf

[36] J. David Large, Broadband Cable Access Networks, Elsevier, 2009 (2009).

[37] H. Wiedemann, Particle accelerator physics, Springer, 2015 (2015).

[38] A. Fattens, L. J. Laslett, Longitudinal coupling impedance of a stationary electron ring in a cylindrical geometry, Particle Accelerators (1972).
URL http://cds.cern.ch/record/1107915/

[39] J. B. Murphy, R. L. Gluckstern, S. Krinsky, Longitudinal wake field for an electron moving on a circular orbit, Part. Accel. 57 (BNL-63090) (1996) 9–64 (1996).
URL http://cds.cern.ch/record/1120287

[40] T. Agoh, K. Yokoya, Calculation of coherent synchrotron radiation using mesh, Physical Review Special Topics-Accelerators and Beams 7 (5) (2004) 054403 (2004). doi:10.1103/PhysRevSTAB.7.054403.

[41] C. Mayes, G. Hoffstaetter, Exact 1d model for coherent synchrotron radiation with shielding and bunch compression, Physical Review Special Topics-Accelerators and Beams 12 (2) (2009) 024401 (2009). doi:10.1103/PhysRevSTAB.12.024401.

[42] A. D. Brynes, P. Smorenburg, I. Akkermans, E. Allaria, L. Badano, S. Brussaard, M. Danailov, A. Demidovich, G. De Ninno, D. Gauthier,G. Gaio5, S. B. van der Geer, L. Giannessi, M. J. De Loos, N. S. Mirian, G. Penco, P. Rebernik, F. Rossi, I. Setija, S. Spampinati, C. Spezzani, M. Trovò, P. H. Williams and S. Di Mitri, Beyond the Limits of 1d Coherent Synchrotron Radiation, arXiv preprint arXiv:1805.05702 (2018). doi:10.1088/1367-2630/aad21d.

[43] D. Zhou, Calculation of CSR Impedance Using Mesh Method [Conference presentation], 2011, ERL2011, KEK, Tsukuba, Japan, https://accelconf.web.cern.ch/ERL2011/talks/wg2017˙talk.pdf.

[44] BIPM, Guide pour l'expression de l'incertitude de mesure, Tech. rep., BIPM (2008).